RSC Advances

PAPER

View Article Online
View Journal | View Issue

Check for updates

Cite this: *RSC Adv.*, 2017, 7, 43708

Received 15th August 2017
Accepted 4th September 2017

DOI: 10.1039/c7ra08993g

rsc.li/rsc-advances

High performance nano-sized $LiMn_{1-x}Fe_xPO_4$ cathode materials for advanced lithium-ion batteries†

Zhihong Lei,[a] Ahmad Naveed,[a] Jingyu Lei,[a] Jiulin Wang,*[a] Jun Yang,[a] Yanna Nuli,[a] Xiangchen Meng[b] and Yunliang Zhao[b]

A series of $LiMn_{1-x}Fe_xPO_4$ ($0 \le x \le 1$) cathode materials with different Mn/Fe ratios have been successfully synthesized by a facile solvothermal method. $LiMn_{1-x}Fe_xPO_4$/C nanoparticles have a width of *ca.* 50 nm and a length of 50–200 nm, coating with a thin carbon layer (*ca.* 2 nm). The effects of iron content on the series of $LiMn_{1-x}Fe_xPO_4$/C materials have been systemically investigated. The homogeneous solid solution and highly conducting nanostructure lead to excellent specific capacities, superior discharge rate capabilities and energy densities for x values in the range of 0.2–0.3. For example, $LiMn_{0.7}Fe_{0.3}PO_4$/C can deliver discharge capacities of 167.6, 153.9 and 139.1 mA h g^{-1} at 0.1C, 1C, and 5C rate, respectively, and shows excellent cycle stability at different rates, and can be considered as a cathode candidate for practical application in advanced lithium-ion batteries.

Introduction

Lithium metal phosphates are promising polyanion cathode materials for lithium-ion batteries, owing to their inherent merits such as low cost, decent electrochemical properties, high stability and environmental benignity. However, these merits have often been undermined by insufficient energy and power delivery due to the extremely low conductivity of phosphates at room temperature and poor Li^+ intercalation/deintercalation kinetics.[1,2]

By doping, carbon coating and nano-sized morphology design, the olivine $LiFePO_4$ (LFP) cathode material has been utilized in power batteries for electric vehicles/hybrid electric vehicles in modern society. Due to its higher potential plateau of 4.1 V *vs.* Li/Li^+ as compared with LFP (3.45 V), olivine $LiMnPO_4$ (LMP) possesses a 20%-higher theoretical energy density than LFP. Moreover, it matches the stability window of conventional carbonate ester-based electrolytes. However, LMP suffers from the drawbacks with even lower intrinsic electronic conductivity ($<10^{-10}$ S cm^{-1}) than those of LFP ($>10^{-8}$ S cm^{-1}) and Jahn–Teller lattice distortion at Mn^{3+} sites, thus leading to lower specific capacity and poorer cycle ability.[3–7]

Up to now, various strategies have been adopted in efforts to promote the electrochemical performance of LMP, such as strict carbon coating, minimizing particles size, and Mn-site substitution. Substituting the Mn site with Fe has been found to be extremely effective for improving the electrochemical performance.[8–10] Various $LiMn_{1-x}Fe_xPO_4$ materials have been reported and the effect of iron substitution is proven.[11–17] For examples, Damen *et al.* reported that $LiMn_{1-x}Fe_xPO_4$ ($x = 0, 0.2, 0.3$) materials were prepared *via* sol–gel, pyrolysis and ball milling steps, in which $LiMn_{0.8}Fe_{0.2}PO_4$ showed the largest discharge capacity of 135 mA h g^{-1} at 0.1C at 50 °C.[18] Hong *et al.* synthesized $LiMn_{1-x}Fe_xPO_4$ ($x = 0, 0.1, 0.2$) nanomaterials *via* a facile solvothermal route in a mixed solvent of water and polyethylene glycol (PEG200) wherein $LiMn_{0.8}Fe_{0.2}PO_4$ sample demonstrated the highest discharge capacity of *ca.* 135 mA h g^{-1} at 0.5C.[19] Liao *et al.* reported that $LiFe_{0.15}Mn_{0.85}PO_4$/C material exhibited the best performance and delivered discharge capacities of 163.1 mA h g^{-1} at 0.1C and 150.3 mA h g^{-1} at 1C in a series of $LiFe_xMn_{1-x}PO_4$/C ($x \le 0.15$) materials which were synthesized by solvothermal reactions in ethylene glycol mixed solutions.[20] A facile polymer-assisted mechanical activation was used to prepare $LiMn_{1-x}Fe_xPO_4$ ($0 \le x \le 1$) by Xiao *et al.* wherein Mn rich $LiMn_{0.75}Fe_{0.25}PO_4$ could deliver 157 mA h g^{-1} at 0.1C.[21] Traditional solid state reaction was also tried to synthesize a series of $LiFe_{1-x}Mn_xPO_4$ materials by Zhang *et al.* in which $LiMn_{0.7}Fe_{0.3}PO_4$ exhibited a highest discharge capacity of 130 mA h g^{-1} at 0.1C.[22]

Although the investigation on $LiMn_{1-x}Fe_xPO_4$/C materials has achieved a great progress, the available capacity under high rate is still unsatisfactory. The electrode kinetics should be improved. In this work, a series of $LiMn_{1-x}Fe_xPO_4$ ($0 \le x \le 1$)

---

[a] *Department of Chemical Engineering, Shanghai Electrochemical Energy Devices Research Centre, Shanghai Jiao Tong University, Shanghai 200240, PR China. E-mail: wangjiulin@sjtu.edu.cn*

[b] *Song Yuan Power Supply Company, Jilin Electric Power Co. LTD, Jilin 138000, PR China*

† Electronic supplementary information (ESI) available: Refined cell parameters of cathode materials, atomic position of $LiMn_{0.7}Fe_{0.3}PO_4$ determined by Rietveld structure refinement, SEM-EDX spectrum, XPS spectrum, Electronic conductivities. See DOI: 10.1039/c7ra08993g

nanomaterials have been successfully synthesized by the solvothermal method, using a new solution system. In addition, a thin carbon layer (*ca.* 2 nm) was further coated on the surface of $LiMn_{1-x}Fe_xPO_4$. Effect of the iron substitution and Mn/Fe ratio on the crystal structure, morphology and electrochemical performance are investigated and discussed in detail. Based on the facile synthetic technology and the excellent electrochemical performance, our work may widen the potential application of $LiMn_{1-x}Fe_xPO_4$ cathode material for advanced lithium-ion battery.

Experimental

Preparation of materials

$LiMn_{1-x}Fe_xPO_4$ (LMFP) ($x = 0$, 0.05, 0.10, 0.15, 0.20, 0.25, 0.30, 0.40, 0.50, 1) were prepared by a facile solvothermal method. Stoichiometric amounts of manganese sulfate monohydrate ($MnSO_4 \cdot H_2O$), ferrous sulfate ($FeSO_4 \cdot 7H_2O$) and ammonium dihydrogen phosphate ($NH_4H_2PO_4$) were dissolved in distilled water and mixed. Ascorbic acid was dispersed in distilled water, then added into the former solution directly as a reducing agent under stirring. N,N′-Dimethylformamide was added carefully. Then lithium hydroxide solution [molar ratio of Li/Mn/Fe = $3 : (1-x) : x$] were dripped slowly and high speed stirring was kept for about 2 h at room temperature to form a gray suspension. The final suspension was sealed into Teflon-lined stainless steel autoclave and heated in an oven at 180 °C for 12 h. After the vessel was cooled down to room temperature, a black reacted suspension was centrifuged at 10 000 rpm for ten minutes and washed several times with deionized water. The claybank powders of LMFP were obtained and dried in vacuum oven at 80 °C.

The LMFP sample was ground to fine powder. 20 wt% sucrose (suc) was mixed with LMFP powder in appropriate ethanol, milled with a high speed of 350 rpm for 6 h (Fritsch, Germany). Afterwards, the mixture was annealed at 550 °C for 4 h in an Ar/H_2 atmosphere ($Ar/H_2 = 95 : 5$, v/v). Finally, the black $LiMn_{1-x}Fe_xPO_4/C$ materials were obtained.

Structure and morphology characterization

The phase compositions of cathode materials were characterized by powder X-ray diffraction analysis (XRD, Bruker D8 Advance) with Cu Kα radiation, operating at 40 kV × 40 mA with scanning rate of $0.25° \text{ min}^{-1}$ or $6° \text{ min}^{-1}$. Rietveld refinement was carried out by GSAS software package.[23] Inductively coupled plasma (ICP, Thermo fisher Scientific iCAP7600) atomic emission spectrometry analysis was used to analyze the elemental composition of Li, Mn, Fe and P. The morphologies were observed using a field emission scanning electron microscope (FESEM, HITACHI S-4800). And the fine structure of materials were observed by a high resolution transmission electron microscope (HRTEM, JEOL 2100F). The carbon contents in the samples were measured by equipment of high frequency infrared ray carbon sulfur analyzer (CS-206 Shanghai Baoying). The electronic conductivities were measured at room temperature by four-probe dc technique (RTS-8, Guangzhou 4 probes). Cylindrical pellets with diameter of 12 mm of synthesized materials were prepared under a pressure of 10 MPa. X-ray photoelectron spectroscopy (XPS, Kratos Axis Ultra DLD spectrometer) was examined to identify the oxidation state of Mn and Fe of composite materials. The data were converted to VAMAS format and processed using Casa XPS software.

Electrochemical measurements

The electrodes consisted of $LiMn_{1-x}Fe_xPO_4/C$ materials, Timcal Super P, and polyvinylidene fluoride (PVDF) in the gravimetric ratio of 8 : 1 : 1. Polyvinylidene fluoride (PVDF) as a binder was dispersed in *N*-methyl-2-pyrrolidone (NMP) firstly. The resultant slurry was coated onto aluminum foil and dried in vacuum oven at 120 °C for about 12 h. The electrode sheet was punched into Φ 12 mm diameter discs as a cathode. The active material loading in the electrodes was *ca.* 1 mg cm^{-2}. The cells were comprised by cathode, lithium foil anode, and separated by a microporous polypropylene membrane (Entek ET20-26). The electrolyte containing 1 M $LiPF_6$ dissolved in ethylene carbonate (EC) and dimethyl carbonate (DMC) (v/v = 1 : 1) was filled into the interspace of cell. Each CR2016 coin-type cell was filled with about 1 mL electrolyte. And the cells were assembled in an argon-filled dry glove box where humidity and oxygen content were controlled less than 1 ppm.

Electrochemical measurements were carried out on Lanhe CT2001A battery test systems. The testing was conducted at constant room temperature (25 °C) in a voltage range of 2.5–4.5 V (*vs.* Li/Li^+) using a constant current–constant voltage (CC–CV) protocol at various charge and discharge rates. The capacities were calculated based on the pure cathode material excluding carbon (theoretical capacity ~170 mA h g^{-1}).

Results and discussion

Crystal structures and ICP element analysis

$LiMnPO_4$ and $LiFePO_4$ belong to the olivine crystal structure and possess similar X-ray diffraction (XRD) patterns. Fig. 1a shows the XRD patterns of the series $LiMn_{1-x}Fe_xPO_4/C$ materials. As expected, they present similar diffraction peaks at adjacent positions, corresponding to orthorhombic with the space group of *Pmnb* (as JCPDS No. 74-0375, $LiMnPO_4$). No crystallized carbon phase was found in the patterns, indicating that carbon exists in amorphous state. The carbon contents of *ca.* 5.3–7.4 wt% were determined by a carbon sulfur analyzer. In detail, it is shown in Table S1.† It is worth noting that the carbon contents of $LiMn_{0.75}Fe_{0.25}PO_4/C$ and $LiMn_{0.7}Fe_{0.3}PO_4/C$ are 7.35 wt% and 5.86 wt% respectively.

As iron proportion increases from 0 to 1, slight peak shift to more 2θ positive values in the diffraction patterns. For example, the peak around 35.14° (2θ) of $LiMnPO_4$ is attributed to crystal plane (111). As x value of $LiMn_{1-x}Fe_xPO_4$ increases, this peak moves toward right up to final position around 35.7°, which is attributed to $LiFePO_4/C$ (Fig. 1b). The fine movement of the peaks of XRD patterns proves that the iron gradually occupies the sites which have been occupied by Mn^{2+} ion. The right shift behavior is associated with the fact that the ion radius of Fe^{2+}

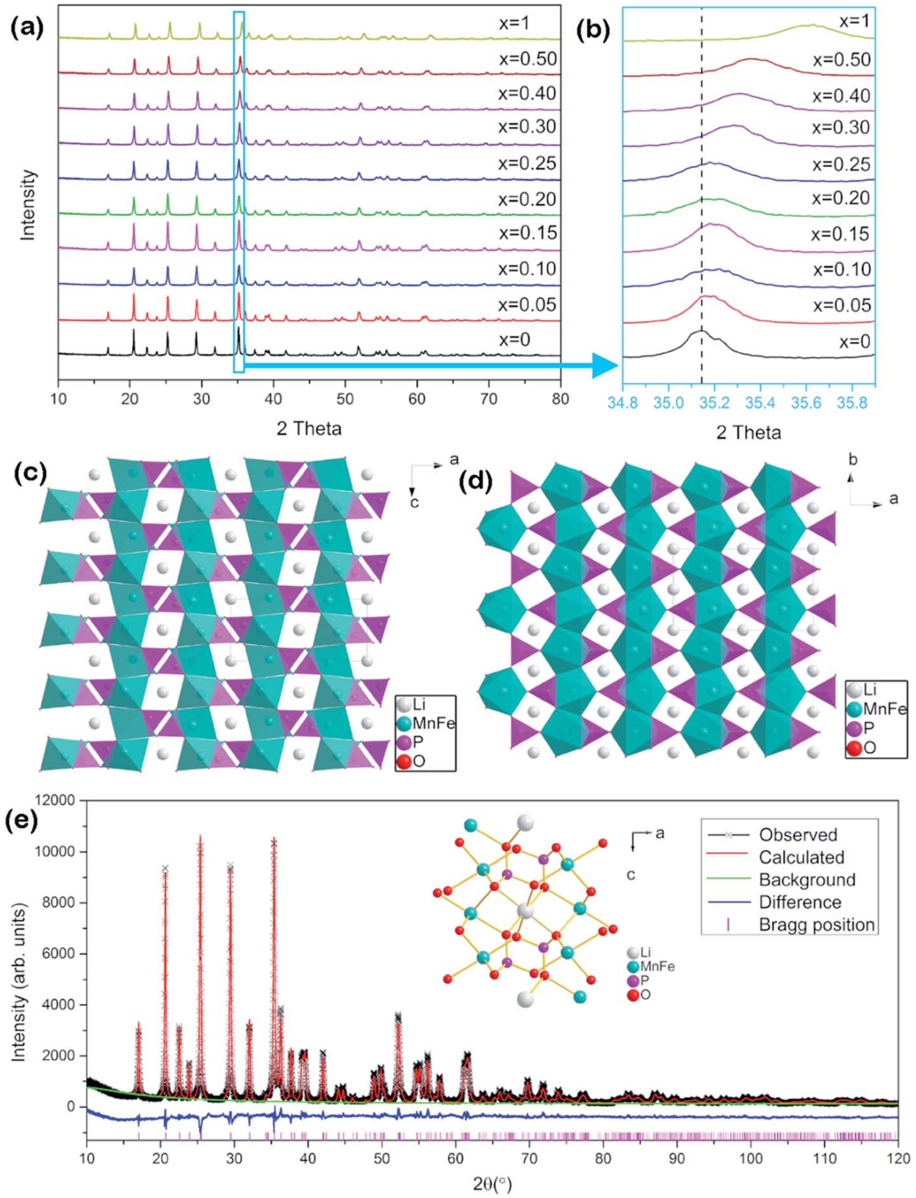

Fig. 1 XRD patterns of $LiMn_{1-x}Fe_xPO_4$/C cathode materials (a and b), the crystal structure of $LiMn_{1-x}Fe_xPO_4$ along *b*-axis (c), along *c*-axis (d), and Rietveld refinement of $LiMn_{0.7}Fe_{0.3}PO_4$/C (e) ($\chi^2 = 3.099$, $R_p = 5.58\%$, $R_{wp} = 7.24\%$).

(0.78 Å) is smaller than Mn^{2+} ion (0.83 Å).[24] The basic crystal lattices parameters of *a*, *b*, *c* and *V* are obviously decreased with the increased iron proportion (Table S1 and Fig. S1†). It gives a strong evidence to prove that the $LiMn_{1-x}Fe_xPO_4$ materials are in a solid solution state.[25]

The crystal structure of $LiMn_{1-x}Fe_xPO_4$ materials is shown in Fig. 1c and d. Polyanionic framework is constructed by the tetrahedral motifs of PO_4 and octahedral groups of LiO_6 and MO_6. The neighboring MO_6 octahedrons share common corners with each other. Neighboring LiO_6 octahedrons share the edge forming chains in the *b*-direction. Each tetrahedral PO_4 shares edge with two neighboring octahedral LiO_6 and shares corner with two other neighboring LiO_6.[26–29] The atomic positions, such as $LiMn_{0.7}Fe_{0.3}PO_4$, were calculated by Rietveld structure refinement (Fig. 1e and Table S2†).[28,30,31] Fe substituting usually happens in 4c-site which is occupied by Mn ion. However, the cation antisite defects could be arisen, so that a slight amount of Fe/Mn ions (<1%) could occupy 4a site, while Li ions occupy 4c site. So the synthesized route should be strictly controlled to limit the antisite defect.[29,31]

The chemical compositions of $LiMn_{0.70}Fe_{0.30}PO_4$ and $LiMn_{0.75}Fe_{0.25}PO_4$ were clarified by ICP element analysis, shown in Table 1. The chemical composition of $LiMn_{0.70}Fe_{0.30}PO_4$ from ICP analysis matched the theoretical molar ratio of Li : Mn : Fe : P as 1.00 : 0.70 : 0.30 : 1.00(±0.009), similar as $LiMn_{0.75}Fe_{0.25}PO_4$. The elemental concentration ratios are generally close to those of the expected compositions.

Table 1 ICP element analysis of selected $LiMn_{1-x}Fe_xPO_4$ ($x = 0.25$, $x = 0.30$)

Elemental (%)	Li	Mn	Fe	P	Intended composition	Observed composition
$x = 0.25$	3.78	22.78	7.494	17.02	$LiMn_{0.75}Fe_{0.25}PO_4$	$Li_{0.9911}Mn_{0.7544}Fe_{0.2442}PO_4$
$x = 0.30$	4.19	23.2	10.1	18.81	$LiMn_{0.70}Fe_{0.30}PO_4$	$Li_{0.9941}Mn_{0.6954}Fe_{0.2979}PO_4$

Morphologies

The morphologies of $LiMn_{1-x}Fe_xPO_4/C$ series were observed by SEM and TEM testing. SEM images in Fig. 2 reveal the nanoparticle distribution of $LiMn_{1-x}Fe_xPO_4/C$ ($x = 0$–1) materials. $LiMn_{1-x}Fe_xPO_4/C$ ($x \neq 0, 1$) samples present the particle sizes with a width of *ca.* 50–80 nm and a length of 60–200 nm, notably smaller than those of $LiMnPO_4/C$ and $LiFePO_4/C$. The $LiMnPO_4/C$ shows two kind of particle shapes (Fig. 2a), in which the larger particle sizes are *ca.* 70 nm in width and 100–360 nm in length, and the smaller ones show shorter length of *ca.* 70 nm. For $LiFePO_4/C$, the primary particles sizes are *ca.* 50 nm in width and *ca.* 100 nm in length, and they are assembled to the secondary particles in spindle shape with *ca.* 100 nm in width and *ca.* 430 nm in length (Fig. 2j). Iron doping into $LiMnPO_4$ leads to smaller particle size. In particular, when iron proportions are in arrange of 0.20–0.30, the particle size distributions are more even. When iron proportion increases to 0.40, some particles become longer. The element analysis was further analyzed by SEM-EDX. The basic composition of $LiMn_{0.75}Mn_{0.25}PO_4/C$ excluding lithium is shown as an example in Fig. S2,† where the molar ratio of Mn : Fe is 15.04 : 5.02, *i.e.* nearly 3 : 1, matching to the structural formula of the molecule.

The TEM observation further confirms the particle sizes of $LiMn_{0.7}Fe_{0.3}PO_4/C$ with the width of *ca.* 40–50 nm and length of 120–160 nm (Fig. 2k). As shown in the Fig. 2l, the particle surface was uniformly coated by a thin carbon layer with the thickness of *ca.* 2 nm. Thus the electronic conductivities can be enhanced greatly after carbon coating. Through the high-resolution TEM, the clear crystal lattice with an interplanar spacing of *ca.* 3.0 Å is displayed, which can be referred to the crystallographic direction of (200) or (121) of $LiMn_{0.7}Fe_{0.3}PO_4/C$.

The $LiMn_{0.7}Fe_{0.3}PO_4/C$ material was further examined by XPS analysis shown in Fig. S3.† Two main peaks at 654 eV and

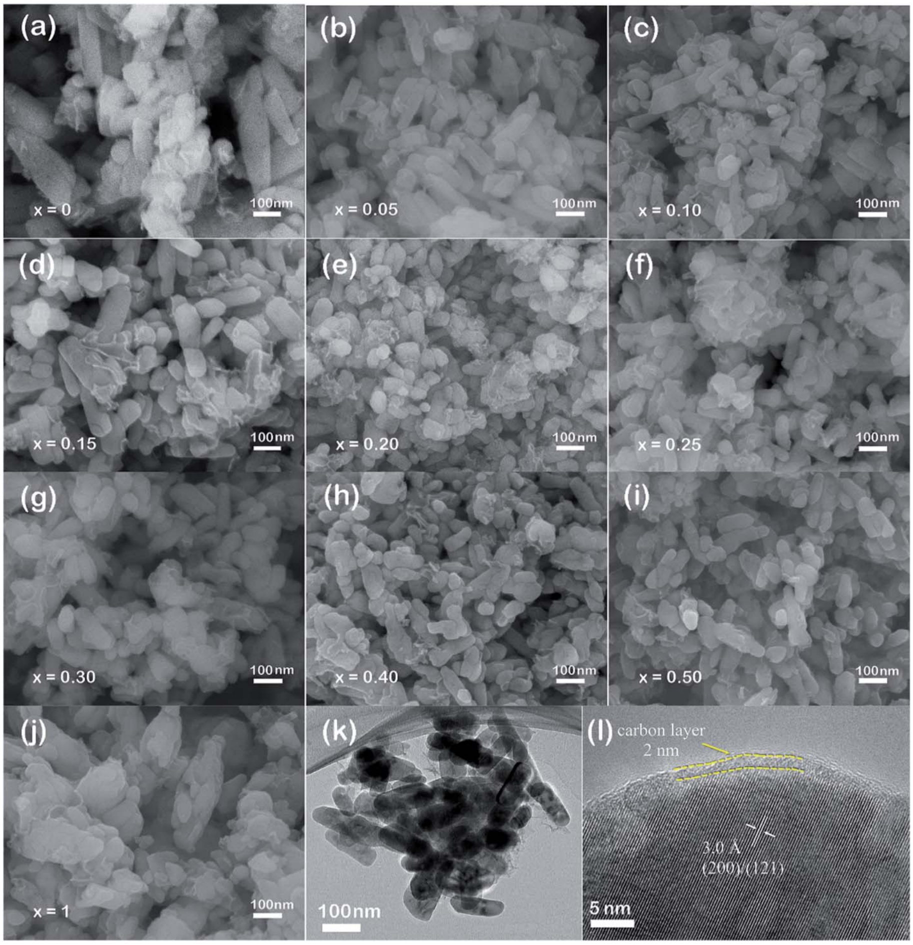

Fig. 2 SEM images of $LiMn_{1-x}Fe_xPO_4/C$ cathode materials (a–j), TEM and HRTEM images of $LiMn_{0.7}Fe_{0.3}PO_4/C$ material (k and l).

642 eV appealed in the spectrum are attributed to Mn $2p_{1/2}$ and Mn $2P_{3/2}$, respectively. There is a "shake-up" satellite peak at 646.7 eV belonged to Mn $2P_{3/2}$. Peaks at 725 eV and 711 eV are attributed to Fe $2P_{1/2}$ and Fe $2P_{3/2}$, respectively.

Electrochemical performances

The voltage–capacity profiles of $LiMn_{1-x}Fe_xPO_4/C$ materials are compared in Fig. 3. As expected, there is only one discharge voltage plateau of $LiMnPO_4/C$ and $LiFePO_4/C$ materials at *ca.* 4.0 V and 3.45 V in the Fig. 3a and f, corresponding to Mn^{3+}/Mn^{2+} and Fe^{3+}/Fe^{2+} reductions, respectively. $LiMnPO_4/C$ and $LiFePO_4/C$ can deliver discharge capacities of 122 mA h g^{-1} and 152 mA h g^{-1} at 0.1C, respectively. While Fe is partially substituted in $LiMnPO_4$, the electrochemical performances are clearly improved as shown in the Fig. 3b–e. Two distinct discharge plateaus are ascribed to manganese and iron ions reduction reactions. With the increased iron content, the low voltage plateau becomes longer. $LiMn_{0.7}Fe_{0.3}PO_4/C$ shows the highest discharge capacities at different rates, such as 167.6 mA h g^{-1} at 0.1C, 160.7 mA h g^{-1} at 0.5C, and 150.6 mA h g^{-1} at 2C. Its electrochemical performances are superior to most of previous reports on similar Mn rich $LiMn_{1-x}Fe_xPO_4/C$ materials (Table 2).[11–22,28,32–41]

The electrochemical cycle performances of $LiMn_{1-x}Fe_xPO_4/C$ at various compositions and current rates are shown in Fig. 4a and b. It can be concluded that partial substitution of iron to manganese in $LiMnPO_4$ can significantly improve the electrochemical performance and $LiMn_{1-x}Fe_xPO_4/C$ materials for x value in the range of 0.20–0.30 show better electrochemical performance. Especially, the $LiMn_{0.7}Fe_{0.3}PO_4/C$ demonstrates the best performances in the cycle, rate and energy density tests. Its capacity retention at 0.1C reaches 94% for 50 cycles with initial discharge capacity of *ca.* 167 mA h g^{-1} which nearly approaches its theoretical value. The electrode exhibits excellent rate capability. In Fig. 4b, it delivers 162.6 and

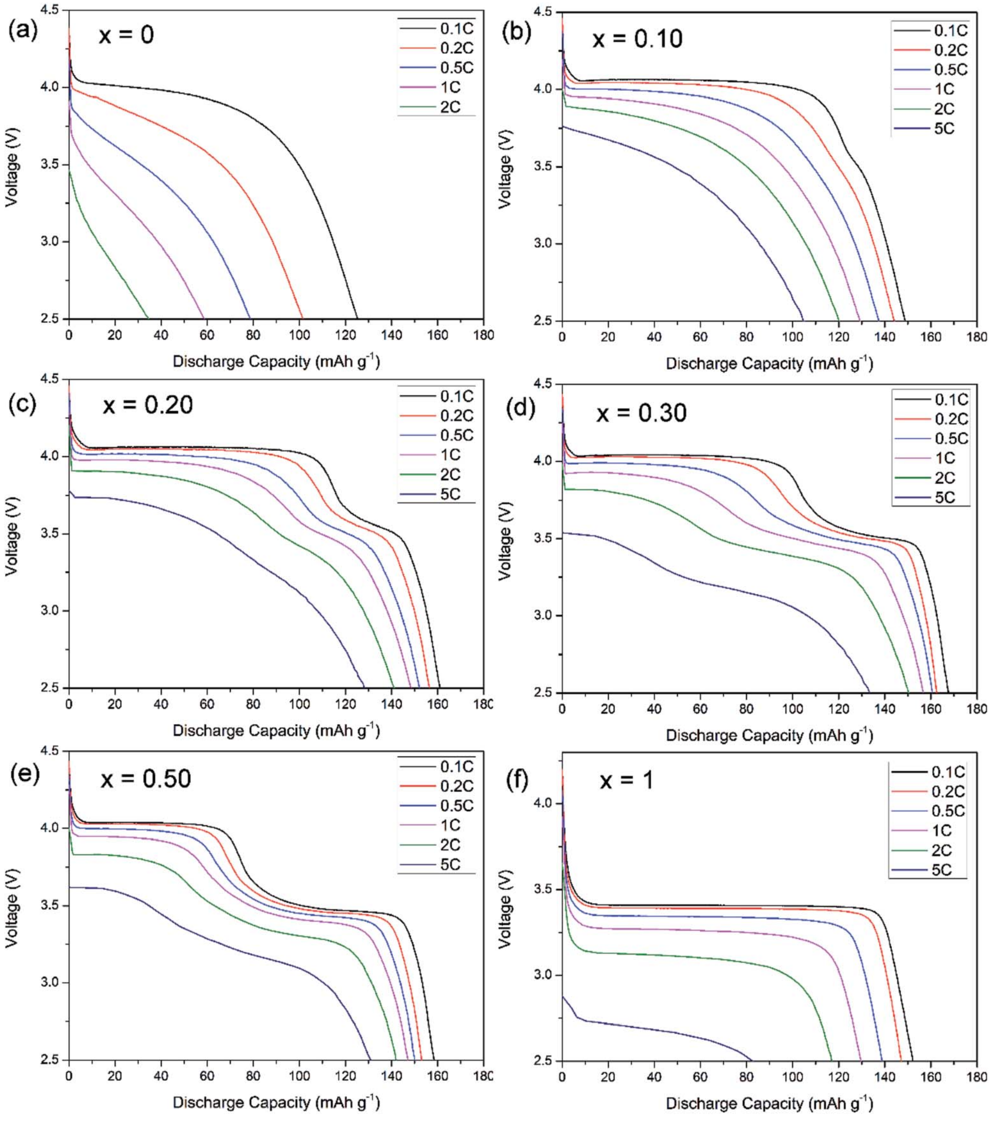

Fig. 3 Discharge rate capability of $LiMn_{1-x}Fe_xPO_4/C$ with (a) $x = 0$, (b) $x = 0.1$, (c) $x = 0.20$, (d), $x = 0.30$, (e) $x = 0.50$, (f) $x = 1$.

Table 2 The comparison of electrochemical performance of the $\mathrm{LiMn_{1-x}Fe_xPO_4}$ (Mn rich) electrodes between this work and reported ones

$\mathrm{LiMn_{1-x}Fe_xPO_4}$ electrodes	Cyclic capacity (mA h g^{-1})	Rate capacity (mA h g^{-1})	Method	Ref.
$\mathrm{LiMn_{0.7}Fe_{0.3}PO_4}$	167.6@0.1C	153.9@1C, 139.1@5C	Solvothermal	This work
$\mathrm{LiMn_{0.75}Fe_{0.25}PO_4}$	161.7@0.1C	141.5@1C, 121.3@5C	Solvothermal	This work
$\mathrm{LiMn_{0.7}Fe_{0.3}PO_4}$	$\sim$150@0.1C	$\sim$135@1C	Solvothermal	12
$\mathrm{LiMn_{0.8}Fe_{0.2}PO_4}$	$\sim$145@0.1C	130@1C	Solvothermal	12
$\mathrm{LiMn_{0.7}Fe_{0.3}PO_4}$	$\sim$120@0.1C	105@1C	Solid state	15
$\mathrm{LiMn_{0.6}Fe_{0.4}PO_4}$	150@0.1C	$\sim$145@1C, 130@5C	Solid state	15
$\mathrm{LiMn_{0.75}Fe_{0.25}PO_4}$	55@0.01C	—	Solvothermal	16
$\mathrm{LiMn_{0.5}Fe_{0.5}PO_4}$	153@0.02C	120@1C	Solvothermal	16
$\mathrm{LiMn_{0.8}Fe_{0.2}PO_4}$	111@0.12C	80@1.2C	Sol–gel	17
$\mathrm{LiMn_{0.9}Fe_{0.1}PO_4}$	142@0.12C	115@1.2C	Sol–gel	17
$\mathrm{LiMn_{0.8}Fe_{0.2}PO_4}$	138@0.1C@50 °C	110@1C@50 °C	Sol–gel	18
$\mathrm{LiMn_{0.8}Fe_{0.2}PO_4}$	165.3@0.05C	142.2@0.5C	Solvothermal	19
$\mathrm{LiMn_{0.85}Fe_{0.15}PO_4}$	163.1@0.1C	150.3@1C, 138@5C	Solvothermal	20
$\mathrm{LiMn_{0.75}Fe_{0.25}PO_4}$	157@0.1C	$\sim$134@1C	Polymer assisted	21
$\mathrm{LiMn_{0.7}Fe_{0.3}PO_4}$	130@0.1C	—	Solid state	22
$\mathrm{LiMn_{0.8}Fe_{0.2}PO_4}$	$\sim$138@0.1C	—	Sol–gel	28
$\mathrm{LiMn_{0.8}Fe_{0.2}PO_4}$	146.5@0.5C	140@1C, 127@5C	Co-precipitation	32
$\mathrm{LiMn_{0.8}Fe_{0.2}PO_4}$	152@0.2C,	146@1C, 130@5C	Solvothermal	33
$\mathrm{LiMn_{0.8}Fe_{0.2}PO_4}$	145@0.2C,	144@1C, 116@5C	Spray dry	33
$\mathrm{LiMn_{0.8}Fe_{0.2}PO_4}$	151@0.1C,	145@1C, 133@5C	Spray dry, CVD	34
$\mathrm{LiMn_{0.8}Fe_{0.2}PO_4}$	161@0.05C	158@0.5C, $\sim$124@5C	Polyol synthesis	35
$\mathrm{LiMn_{0.8}Fe_{0.2}PO_4}$	162@0.1C,	145@1C	Solid state	36
$\mathrm{LiMn_{0.75}Fe_{0.25}PO_4}$	132@0.1C	120@1C	Co-precipitation	37
$\mathrm{LiMn_{0.7}Fe_{0.3}PO_4}$	160@0.05C	—	Sol–gel	38
$\mathrm{LiMn_{0.7}Fe_{0.3}PO_4}$	$\sim$136@0.5C	107@5C	Solid state	39
$\mathrm{LiMn_{0.75}Fe_{0.25}PO_4}$	156@0.1C,	153@1C, $\sim$136@5C	Microwave	40
$\mathrm{LiMn_{0.8}Fe_{0.2}PO_4}$	142@0.1C	103@1C, 69@5C	Sol–gel	41

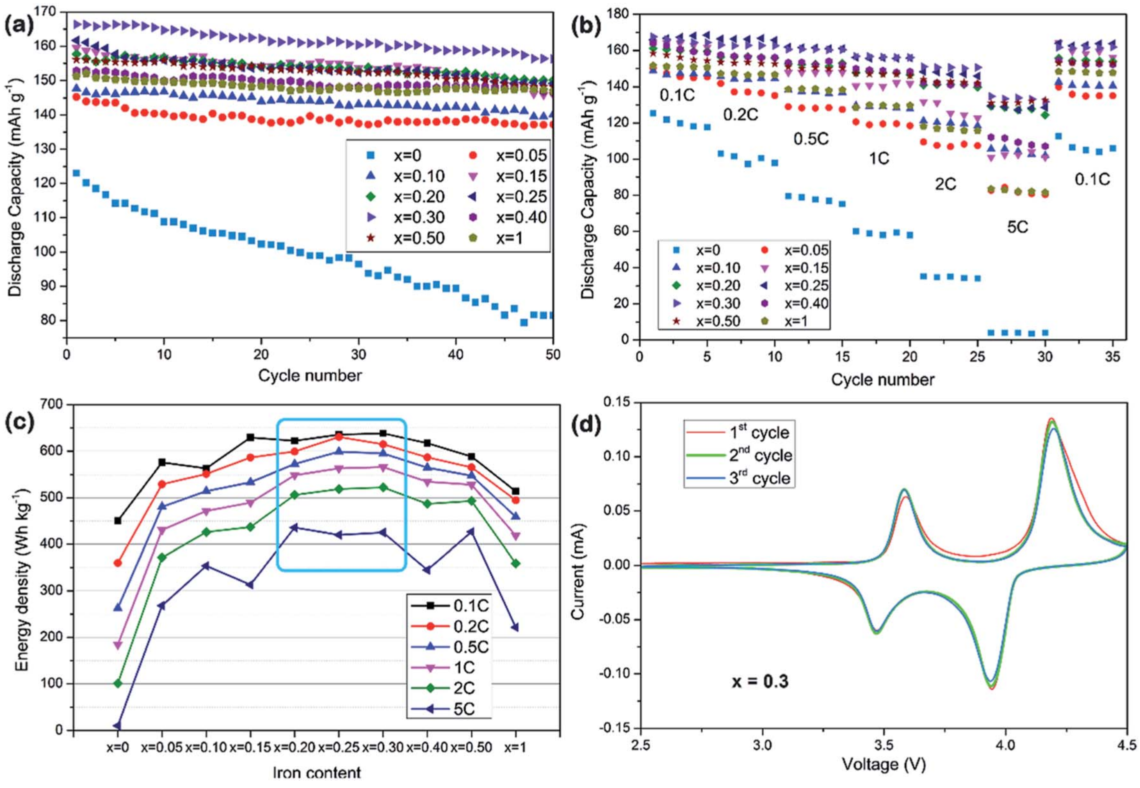

Fig. 4 Cyclic performance of $\mathrm{LiMn_{1-x}Fe_xPO_4/C}$ materials at 0.1C (a), rate properties of $\mathrm{LiMn_{1-x}Fe_xPO_4/C}$ materials (b), and energy density at different iron proportion in different rate (c), cyclic voltammograms of $\mathrm{LiMn_{0.7}Fe_{0.3}PO_4/C}$ at scanning rate of 0.1 mV s^{-1} (d).

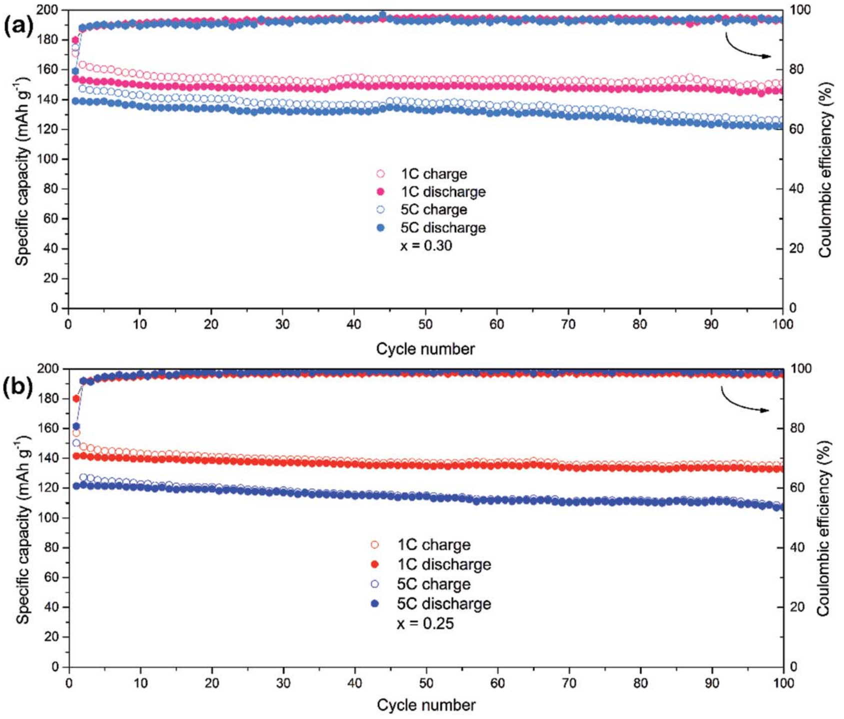

Fig. 5 Cyclic performances of $LiMn_{1-x}Fe_xPO_4/C$ ($x = 0.3, 0.25$) and at 1C and 5C rate.

150.6 mA h g^{-1} at 0.2C and 2C, respectively. It is notable that higher iron content, such as $x = 0.40$, or even for $LiFePO_4$, will degrade cycle capacity and rate capability. Here the particle size and carbon coating uniformity may be played an important role in relate electrochemical performances. In view of discharge voltage and the corresponding capacity, $LiMn_{1-x}Fe_xPO_4/C$ ($x = 0.25$–0.30) present a higher energy density (Fig. 4c). The $LiMn_{0.7}Fe_{0.3}PO_4/C$ reaches the energy density of 638.3 W h g^{-1} at 0.1C, 24% higher than that of $LiFePO_4/C$ (513.8 W h g^{-1}), which could be considered as a candidate cathode for power lithium-ion batteries.

The cyclic voltammetry result of $LiMn_{0.7}Fe_{0.3}PO_4/C$ is investigated as an example at scanning rate of 0.1 mV s^{-1} in Fig. 4d. Two pairs of peaks are clearly shown at 4.19/3.94, 3.58/3.48 V, which attributed to oxidation and reduction peaks of Mn^{3+}/Mn^{2+}, Fe^{3+}/Fe^{2+}, respectively. The sharper current peaks and symmetry redox peaks indicate the kinetics of Li^+ intercalation/deintercalation are greatly ameliorated.

The $LiMn_{0.75}Fe_{0.25}PO_4/C$ and $LiMn_{0.7}Fe_{0.3}PO_4/C$ materials are selected for a further evaluation of the cycle stability at high rates (Fig. 5). The initial discharge capacities of $LiMn_{0.7}Fe_{0.3}PO_4/C$ at rate of 1C and 5C are 153.9 and 139.1 mA h g^{-1}. After 100th cycles at rate of 1C and 5C, $LiMn_{0.7}Fe_{0.3}PO_4/C$ still delivers 146 and 122.3 mA h g^{-1} with the retention of 95% and 88%, respectively. While $LiMn_{0.75}Fe_{0.25}PO_4/C$ shows similar cyclability properties, but its capacity is lower as shown in Fig. 5b. The initial discharge capacities at rate of 1C and 5C are 141.5 and 121.3 mA h g^{-1}, respectively.

The electronic conductivities of $LiMn_{0.7}Fe_{0.3}PO_4/C$ and $LiMn_{0.75}Fe_{0.25}PO_4/C$ were tested by four-probe dc technique which showed the values of *ca.* 5.8×10^{-5} S cm^{-1} and 3.1×10^{-5} S cm^{-1} respectively (Table S3†).[42,43] The former one owns better conductivity property, benefiting and corresponding with it superior electrochemical performance evidently.

The electrochemical performances of the materials are excellent, even superior to that the aforementioned reports as compared in Table 2. The high capacity, excellent cycle and rate performances can be attributed to short Li^+ ions diffusion pathway of the nano-sized particles, thin and even carbon layer coating for enhanced electronic conductivities and iron ions substitution for depressed John–Teller effect.

Conclusion

A series of $LiMn_{1-x}Fe_xPO_4/C$ ($0 \leq x \leq 1$) cathode materials for lithium-ion batteries have been successfully synthesized *via* a facile solvothermal assisted sucrose calcination. $LiMn_{1-x}Fe_xPO_4$ materials belong to olivine solid-solution structure where Fe^{2+} ions partially substitute Mn^{2+} ions site in the crystal lattice. The $LiMn_{1-x}Fe_xPO_4/C$ ($x \neq 0, 1$) samples show nano-sized particle shapes with a width of *ca.* 50–80 nm, length of 60–200 nm, and thin carbon layer (*ca.* 2 nm) coating on the surface, while the $LiMnPO_4/C$ and $LiFePO_4/C$ present slightly larger particles size or aggregated structure. In all the tested materials, $LiMn_{1-x}Fe_xPO_4/C$ ($x = 0.20$–0.30) demonstrate superior electrochemical performances, such as 167.6 mA h g^{-1} at 0.1C, 153.9 mA h g^{-1} at 1C and 139.1 mA h g^{-1} at 5C for $LiMn_{0.7}Fe_{0.3}PO_4/C$. The high capacity and impressive rate performance can be attributed to nanoscale and even particle distribution, uniform thin-layer carbon coating and iron ions substitution. They are promising for practical application in power lithium-ion batteries.

Conflicts of interest

There are no conflicts to declare.

Acknowledgements

This work was supported by the National Natural Science Foundation of China (51272156, 21373137, 21333007), City Committee of Science and Technology Project of Shanghai (14JC1491800) and New Century Excellent Talents in University (NCET-13-0371).

Notes and references

1 C. Masquelier and L. Croguennec, *Chem. Rev.*, 2013, **113**, 6552–6591.
2 M. S. Whittingham, *Chem. Rev.*, 2014, **114**, 11414–11443.
3 N. N. Bramnik and H. Ehrenberg, *J. Alloys Compd.*, 2008, **464**, 259–264.
4 S. M. Oh, H. G. Jung, C. S. Yoon, S. T. Myung, Z. H. Chen, K. Amine and Y. K. Sun, *J. Power Sources*, 2011, **196**, 6924–6928.
5 K. P. Wu, G. R. Hu, Z. D. Peng, Z. J. Zhang, Y. B. Cao and K. Du, *RSC Adv.*, 2015, **5**, 95020–95027.
6 G. Li, P. C. Wu, C. H. Luo, Q. Cui, G. X. Wang and K. P. Yan, *J. Energy Chem.*, 2015, **24**, 375–380.
7 Y. Zhang, H. J. Zhang, Y. Y. Feng, L. Fang and Y. Wang, *Small*, 2016, **12**, 516–523.
8 J. Hong, F. Wang, X. L. Wang and J. Graetz, *J. Power Sources*, 2011, **196**, 3659–3663.
9 M. Jo, H. Yoo, Y. S. Jung and J. Cho, *J. Power Sources*, 2012, **216**, 162–168.
10 L. G. Wang, P. J. Zuo, G. P. Yin, Y. L. Ma, X. Q. Cheng, C. Y. Du and Y. Z. Gao, *J. Mater. Chem. A*, 2015, **3**, 1569–1579.
11 J. M. Bai, J. Hong, H. Y. Chen, J. Graetz and F. Wang, *J. Phys. Chem. C*, 2015, **119**, 2266–2276.
12 L. J. Hu, B. Qiu, Y. G. Xia, Z. H. Qin, L. F. Qin, X. F. Zhou and Z. P. Liu, *J. Power Sources*, 2014, **248**, 246–252.
13 J. Molenda, W. Ojczyk, K. Swierczek, W. Zajac, F. Krok, J. Dygas and R. S. Liu, *Solid State Ionics*, 2006, **177**, 2617–2624.
14 M. Yoncheva, V. Koleva, M. Mladenov, M. Sendova-Vassileva, M. Nikolaeva-Dimitrova, R. Stoyanova and E. Zhecheva, *J. Mater. Sci.*, 2011, **46**, 7082–7089.
15 S. Y. Yan, C. Y. Wang, R. M. Gu, S. Sun and M. W. Li, *J. Alloys Compd.*, 2015, **628**, 471–479.
16 K. Saravanan, V. Ramar, P. Balaya and J. V. Vittal, *J. Mater. Chem.*, 2011, **21**, 14925–14935.
17 S. Novikova, S. Yaroslavtsev, V. Rusakov, A. Chekannikov, T. Kulova, A. Skundin and A. Yaroslavtsev, *J. Power Sources*, 2015, **300**, 444–452.
18 L. Damen, F. De Giorgio, S. Monaco, F. Veronesi and M. Mastragostino, *J. Power Sources*, 2012, **218**, 250–253.
19 Y. Hong, Z. L. Tang, Z. J. Hong and Z. T. Zhang, *J. Power Sources*, 2014, **248**, 655–659.
20 L. H. Liao, H. T. Wang, H. Guo, P. Y. Zhu, J. Xie, C. H. Jin, S. C. Zhang, G. S. Cao, T. J. Zhu and X. B. Zhao, *J. Mater. Chem. A*, 2015, **3**, 19368–19375.
21 P. F. Xiao, B. Ding, M. O. Lai and L. Lu, *J. Electrochem. Soc.*, 2013, **160**, A918–A926.
22 B. Zhang, X. J. Wang, H. Li and X. J. Huang, *J. Power Sources*, 2011, **196**, 6992–6996.
23 B. H. Toby, *J. Appl. Crystallogr.*, 2001, **34**, 210–213.
24 A. Osnis, M. Kosa, D. Aurbach and D. T. Major, *J. Phys. Chem. C*, 2013, **117**, 17919–17926.
25 A. Iturrondobeitia, A. Goni, I. G. de Muro, L. Lezama, C. J. Kim, M. Doeff, J. Cabana and T. Rojo, *Inorg. Chem.*, 2015, **54**, 2671–2678.
26 A. Yamada, Y. Takei, H. Koizumi, N. Sonoyama and R. Kanno, *Chem. Mater.*, 2006, **18**, 804–813.
27 C. A. J. Fisher, V. M. Hart Prieto and M. Saiful Islam, *Chem. Mater.*, 2008, **20**, 5907–5915.
28 I. Seo, B. Senthilkumar, K. H. Kim, J. K. Kim, Y. S. Kim and J. H. Ahn, *J. Power Sources*, 2016, **320**, 59–67.
29 S. Kandhasamy, K. Nallathamby and M. Minakshi, *Prog. Solid State Chem.*, 2012, **40**, 1–5.
30 J. Schoiber, G. Tippelt, G. J. Redhammer, C. Yada, O. Dolotko, R. J. F. Berger and N. Hüsing, *Cryst. Growth Des.*, 2015, **15**, 4213–4218.
31 K. Jensen, M. Christensen, C. Tyrsted and B. B. Iversen, *J. Appl. Crystallogr.*, 2011, **44**, 287–294.
32 W. C. Yang, Y. J. Bi, Y. P. Qin, Y. Liu, X. H. Zhang, B. C. Yang, Q. Wu, D. Y. Wang and S. Q. Shi, *J. Power Sources*, 2015, **275**, 785–791.
33 L. T. Yang, Y. G. Xia, L. F. Qin, G. X. Yuan, B. Qiu, J. L. Shi and Z. P. Liu, *J. Power Sources*, 2016, **304**, 293–300.
34 L. T. Yang, Y. G. Xia, X. Fan, L. F. Qin, B. Qiu and Z. P. Liu, *Electrochim. Acta*, 2016, **191**, 200–206.
35 H. Xu, J. Zong, F. Ding, Z. W. Lu, W. Li and X. J. Liu, *RSC Adv.*, 2016, **6**, 27164–27169.
36 H. C. Shim, S. Bang, D. M. Yoon, Y. S. Kong and T. Yu, *J. Alloys Compd.*, 2015, **649**, 1315–1322.
37 Y. Satou, S. Komine, S. Takai and T. Yao, *ECS Electrochem. Lett.*, 2015, **4**, A37–A40.
38 S. S. Li, Z. Su, A. Muslim, X. K. Jiang and X. Y. Wang, *Ceram. Int.*, 2015, **41**, 11132–11135.
39 B. Ding, P. F. Xiao, G. Ji, Y. Ma, L. Lu and J. Y. Lee, *ACS Appl. Mater. Interfaces*, 2013, **5**, 12120–12126.
40 M. S. Kim, J. P. Jegal, K. C. Roh and K. B. Kim, *J. Mater. Chem. A*, 2014, **2**, 10607–10613.
41 B. Z. Li, Y. Wang, L. Xue, X. P. Li and W. S. Li, *J. Power Sources*, 2013, **232**, 12–16.
42 Y. Y. Cai, D. Y. Zhang, C. K. Chang, Z. M. Sheng and K. J. Huang, *Ionics*, 2016, **22**, 1011–1019.
43 P. R. Kumar, M. Venkateswarlu, M. Misra, A. K. Mohanty and N. Satyanarayana, *Ionics*, 2013, **19**, 461–469.